Dispersion and birefringence of irregularly microstructured fiber with an elliptic core

Hyoung-Gyu Choi,[1,2] Chul-Sik Kee,[2,*] Kyung-Han Hong,[2] JaeHee Sung,[2] Soan Kim,[2] Do–Kyeong Ko,[2] Jongmin Lee,[2] Jae–Eun Kim,[1,*] and Hae Yong Park[1]

[1]Department of Physics, Korea Advanced Institute of Science and Technology, Daejeon 305-701, South Korea
[2]Nanophotonics Laboratory, Advanced Photonics Research Institute, GIST, Gwangju 500-712, South Korea

*Corresponding authors: cskee@gist.ac.kr and jekim@kaist.ac.kr

Received 8 May 2007; revised 20 July 2007; accepted 20 July 2007;
posted 27 July 2007 (Doc. ID 82835); published 7 December 2007

We have investigated the dispersion and birefringence of an irregularly microstructured fiber with an elliptic silica core and irregular airholes. The polarization-dependent output power through the fiber reveals two well-defined principal-axis modes despite the irregularity of airholes. The dispersion of the fiber is measured in the range of 680 to 1000 nm using the Mach–Zehnder interferometric technique with sub-10 fs laser pulses, which yield two zero dispersion wavelengths at 683 and 740 nm for the two principal modes, respectively. The birefringence measured using the wavelength scanning method is about 0.0055 at 800 nm. It is also demonstrated that this irregularly microstructured fiber with high birefringence and short zero dispersion wavelength is useful for the one-octave-spanning supercontinuum generation suitable for an *f*–2*f* interferometric system.

OCIS codes: 060.2270, 260.1440, 260.2030.

1. Introduction

Air-silica microstructured fibers are of significant research interest because they can tightly confine the light in the core due to the high index contrast between the core and the cladding. Moreover, the design freedom allows one to vary the optical parameters, such as dispersion and nonlinearity, with ease [1]. The high nonlinearity induced by the strong confinement of the light and the shift of zero dispersion wavelength (ZDW) of microstructured fibers below 800 nm can bring about two-octave-spanning of the supercontinuum (SC) spectrum [2]. Many theories have explained well the physical origin of SC generation and shown that the dispersion properties of microstructured fibers are one of the most important parameters [3–5]. Thus, it is a prerequisite to properly characterize the dispersion of microstructured fibers for applications as a light source in Raman spectroscopy, optical coherence tomography, and the frequency metrology [6–8].

Microstructured fibers with an elliptic core could be useful in generating controllable SC because the anisotropic dispersion property given by the elliptic core allows various spectral contents of SC through the variation of the input-beam polarization. The elliptic core microstructured fibers can be fabricated by using irregularly arranged airholes, rather than a regular array of airholes. To the best of our knowledge, the dispersion property and birefringence of an irregularly microstructured elliptic core fiber (IMEF), a microstructured fiber with an elliptic core surrounded by irregularly arranged airholes of various sizes, has rarely been investigated [4].

In this paper, we investigate experimentally and numerically the properties of an IMEF, including the principal guiding modes, the dispersion of the modes, the birefringence, and the SC spectra. The polarization-dependent output power through an IMEF reveals two well-defined principal-axis modes, which are predicted by the finite-element method simulation. The Mach–Zehnder (MZ) interferometric method [9,10] and the wavelength scanning method [11,12] are employed to measure the dispersion and the birefringence, respectively. The ZDWs for two

0003-6935/07/358493-06$15.00/0

principal modes are 683 and 740 nm. The birefringence is an order of 10^{-3} around 800 nm, which is one order of magnitude larger than the values for conventional polarization-maintaining fibers. We also show that the SC spectrum generated with the IMEF can be applicable to an f–$2f$ interferometric system.

2. Irregularly Microstructured Fiber and Its Principal Modes

Figure 1 shows the scanning electron microscope (SEM) image of the cross section of the IMEF, which is made of pure silica. The elliptic core surrounded by airholes has a long axis of about 2 μm and a short axis of about 1 μm. Airholes of various sizes that are irregularly arranged around the core act as a cladding region with a low effective index. The largest (smallest) diameter of six airholes adjacent to the core is about 1.7 (0.8) μm. Figure 2 shows two fundamental guiding mode profiles of the IMEF, which are obtained numerically by the finite-element method at the source wavelength of 800 nm [13]. The cross section of the IMEF was divided into distinct homogeneous finite elements of different sizes, and the Maxwell's equations can be solved with the conditions of continuity at the boundary of each finite element to get the propagation modes of the IMEF. Figure 2(a) represents a long axis mode whose electric field (E-field) direction is parallel to the long axis of the core and (b) a short axis mode whose E-field direction is orthogonal to that. One can see that their spatial distributions of power density have the elliptic shape.

Shown in Fig. 3(a) is the diffraction image near the end facet of the IMEF experimentally observed with an Si-based CCD camera and a 60× objective lens. The contours of airholes are intentionally depicted for easy recognition. The elliptic core is clearly seen, and small spots adjacent to airholes also carry small portions of energy. The far-field images taken using a 30× objective lens, a white screen, and a digital camera are shown in Figs. 3(b) and 3(c), depending on the polarization of input pulse along the two principal axes. Though the near-field image is complicated, the far-field images have good elliptic shape with an aspect ratio of about 2. The white arrows in Fig. 3 indicate the long axis of the IMEF, which is derived from the near-field image, Fig. 3(a). Note that the long axis of the far-field image is along the short axis of the near-field image, that is, the short axis of the elliptic core. The pulse spreads out at wider angles in the direction of the short axis with a narrower aperture than the long axis direction, and that agrees with the general diffraction theory [14]. The red arrows in Figs. 3(b) and 3(c) show the E-field direction of the input pulse, which is confirmed by the linear polarizer. According to the E-field direction with respect to the shape of the elliptic core, we denominate the two modes of Figs. 3(b) and 3(c) as the long axis mode and the short axis mode, respectively.

Figure 4 shows the dependence of the output power with respect to each mode on θ, the angle between the polarization direction of the input pulse and the long axis of the core. The cyan solid (blue dashed) curve represents the intensity of long (short) axis mode in the output power as a function of θ, which is obtained by aligning the output linear polarizer with the long (short) axis of the IMEF. The output intensities have good symmetry of 180°. The intensities of the long and the short axis modes have a phase difference of 90°, which means that the principal axes of the fiber are orthogonal to each other. The well-symmetrized output intensities show that the irregular airholes are useful in making the highly elliptic core.

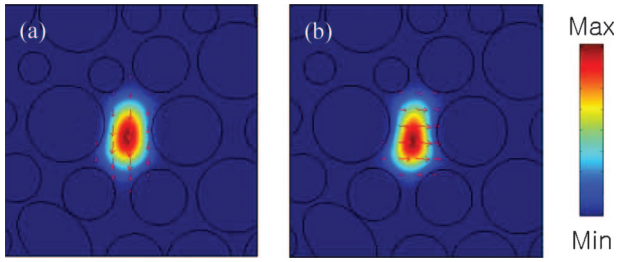

Fig. 2. (Color online) Simulated profiles of the two fundamental guiding modes of the IMEF. Spatial distributions of power density are shown. Transverse-E-field vectors are indicated by red arrows: (a) long axis mode, whose polarization direction is parallel to the long axis of the elliptic core, and (b) short axis mode, whose polarization direction is parallel to the short axis of the elliptic core.

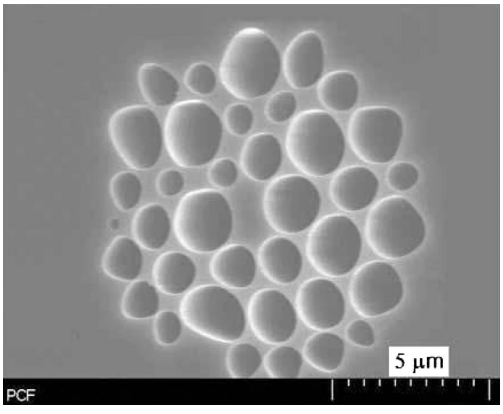

Fig. 1. SEM image of the cross section of the IMEF used in our experiment.

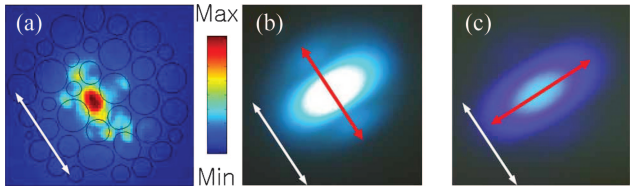

Fig. 3. (Color online) (a) Near-field pattern and (b)–(c) far-field patterns of the guided modes of the IMEF. Contour of airholes in (a) is shown for the convenience. In (b) and (c), white arrows indicate the long axis of the elliptic core and the red arrows the E-field directions, respectively.

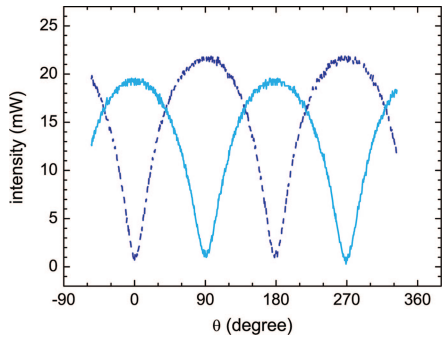

Fig. 4. (Color online) Dependence of the measured output power on θ, the angle between the polarization of input pulse and the long axis of the core. Long and short axis modes are indicated by the cyan solid and blue dashed curves, respectively.

3. Measurement of Dispersion

Various techniques like the pulse delay [15], phase-shift [16], and interferometric method have been developed to measure the dispersion of optical fibers. Especially, the interferometric method in the spectral domain gives accurate dispersion with a short fiber. Our experimental setup is shown in Fig. 5. Sub-10 fs pulses are of benefit to get an interferometric spectrum as wide as possible. A homemade sub-10 fs Ti:sapphire laser with an ultrabroadband spectrum is utilized for the dispersion measurement of the IMEF and to generate SC at the wavelength at approximately 800 nm. The half-wave plate (HW)1 is used as a power attenuator in combination with a Faraday isolator (FI). The FI not only prevents the backreflection from the IMEF but also reduces the peak power of the input pulse by its dispersion effect, broadening the pulse up to 200 fs with a positive chirp. While an excessive peak power causes the generation of nonlinear effects such as self-phase modulation due to the high nonlinearity of the small core, an insufficient power makes it difficult to measure the interference fringes. Thus, the input power should be properly controlled using the HW1. The measured input power after the FI was approximately 120 mW, and at this power nonlinear effect is found to be negligible because no newly generated spectral components appeared after the propagation through the IMEF. Because the reference pulse should have the same direction of polarization with the signal pulse to make interferences, the polarization direction of the reference pulse is controlled using the HW3, and checked by a linear polarizer.

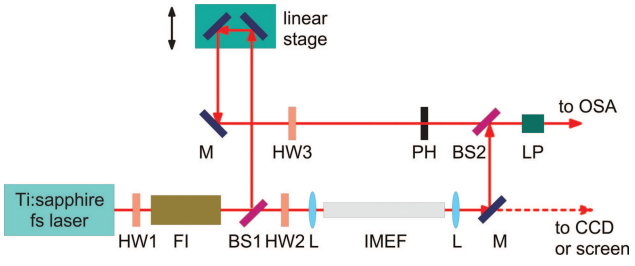

Fig. 5. (Color online) Mach–Zehnder interferometry setup. LP: linear polarizer, M: mirror, BS: beam splitter, FI: Faraday isolator, HW: half-wave plate, PH: pinhole, L: lens.

The interference pattern can be expressed as follows. The signal and reference fields are defined as:

$$E_s = A_s \exp(i\beta_s l_s - i\omega t) \text{ and } E_r = A_r \exp(i\beta_r l_r - i\omega t), \tag{1}$$

respectively, where the coefficients A_s, A_r are the amplitudes, β_s and β_r the wave numbers, l_s and l_r the propagation lengths of the signal arm and the reference arm, respectively, and t the time. The spectrum of the output pulse of the MZ interferometer is given by:

$$I = |A_s|^2 + |A_r|^2 + 2A_s A_r^* \cos\Phi, \tag{2}$$

where Φ is the phase difference between the pulses, which pass through the reference arm and the signal arm. The time delay of traveling through two arms as a function of frequency is obtained by:

$$\tau = \frac{\partial\Phi}{\partial\omega} = \frac{\partial\beta_s}{\partial\omega} l_s - \frac{\partial\beta_r}{\partial\omega} l_r. \tag{3}$$

When the IMEF is placed in the signal arm, the time delay due to the IMEF, $(\partial\beta_{\text{IMEF}}/\partial\omega)L$, is added to the time delay, where β_{IMEF} is the wavenumber of the pulse propagating through the IMEF of length L. On the assumption that the pulse propagates in the air with the constant speed c regardless of the frequency, the time delay is expressed as:

$$\tau = \frac{\partial\beta_{\text{IMEF}}}{\partial\omega} L + \text{const}, \tag{4}$$

where const $= (l_s - l_r)/c$. It means that the derivative of phase with respect to the frequency gives the time delay, which shows the dispersion properties of the IMEF.

We used a 15 cm long IMEF in this experiment, and the interference fringes and the measured time delays are drawn in Fig. 6 together with the dispersion parameter D. Generally, a longer IMEF would produce a larger temporal broadening of the pulses, and the error range in the values of time delay for given wavelength gets reduced for a longer IMEF. However, in our measurement we could not get clear interference fringes with a longer IMEF. It might be that the spectral noise due to the nonlinear effects such as cross-phase modulation and four-wave mixing generates new spectral components. To reduce the noise, the experimental data are accumulated, varying the length of the reference arm in steps of 50 μm. In addition, we tune the laser oscillator so that we can get a high signal-to-noise ratio in the shorter wavelength region though the sub-10 fs pulse has a wide spectral bandwidth. Figure 6(a) shows two interference fringes of the long axis mode for the full laser bandwidth and for the short-wavelength spec-

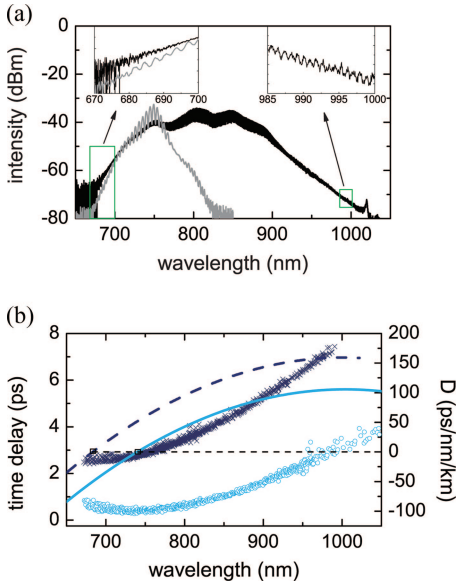

Fig. 6. (Color online) (a) Detected interference fringes obtained using the MZ interferometric method. Black curve shows the bandwidth of the sub-10 fs pulse, and the modified input pulse in the shorter wavelength region as shown in the gray line was used to get a clearer fringe pattern. Insets show the magnified fringe patterns of the boxed spectral regions. (b) Cyan circle and blue cross data points are measured time delays with the MZ interferometric method for the long axis mode and the short axis mode, respectively. Obtained dispersion parameters D are shown in the solid and dashed curves of corresponding colors.

tral range. The interferometric spectrum obtained using the sub-10 fs pulse is shown in black and the result obtained using the adjusted pulses is shown in gray, respectively. The total interferometric spectrum ranges from 680 to 1000 nm. The cyan circle and blue cross data points in Fig. 6(b) indicate the time delays for the long axis mode and the short axis mode, respectively, which are calculated as $\tau(\bar{\omega}) \approx 2\pi/\Delta\omega$, where $\Delta\omega$ is the frequency difference between the adjacent peaks in the interference fringe, and $\bar{\omega}$ is the corresponding center frequency. It shows that the long axis mode has higher group velocity than the short axis mode. The dispersion parameter ($D = d\tau/\lambda/L$) in the figure was obtained from a third-order polynomial fit of the time delay and is shown by the cyan solid (blue dashed) curve for the long (short) axis mode, exhibiting the ZDW of 740 nm (683 nm). D increases in proportion to the wavelength until 1000 nm and then decreases at longer wavelengths, which suggests that there may be a second ZDW at a longer wavelength [17,18]. The big difference between the two ZDWs of the long and short axis modes enables us to obtain highly diverse SC spectra by varying the direction of the linear polarization of the input pulse. Note that the short ZDW can yield an ultrabroad SC spectrum.

4. Measurement of Birefringence

We also characterized the birefringence of the IMEF using the wavelength scanning method, whose experimental setup is shown in Fig. 7. The input pulse with approximately 10 fs pulse width was employed in this experiment, and the average power after the FI was about 80 mW. The HW1 and the FI in Fig. 7 play the same roles as in the setup shown in Fig. 5. Using the HW2, the direction of the linearly polarized input pulse should be oriented at 45° with respect to the principal axes of the IMEF, which makes the input pulses propagate in the two fundamental modes. After the propagation through the fiber, a time delay is generated between the two pulses propagating in each fundamental mode due to the different effective group indices. The time delay results in interference fringes in the spectral domain, and a linear polarizer is used to analyze it. Due to the high ellipticity of the core and corresponding high birefringence, relatively short IMEF is necessary to be able to observe interference fringes in the spectral domain. A long IMEF induces too much time delay between two pulses and thus significantly reduces the fringe spacings. An 11.9 cm long IMEF is used in this experiment.

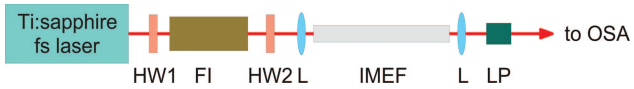

Fig. 7. (Color online) Interferometry setup of the wavelength scanning method. LP: linear polarizer, FI: Faraday isolator, HW: half-wave plate, L: lens.

Figure 8(a) shows the measured interference fringe, and a part of it is magnified in the inset. The

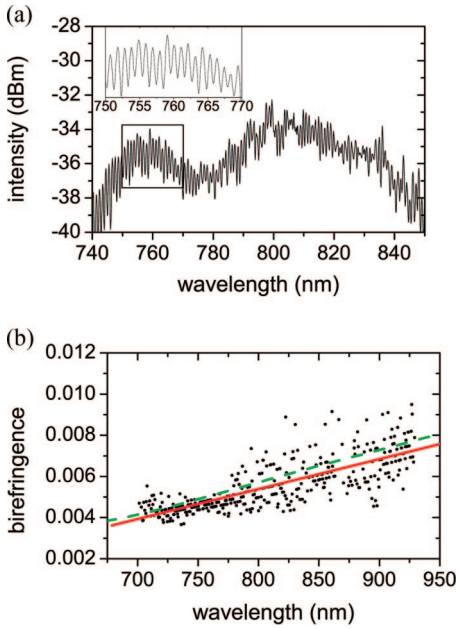

Fig. 8. (Color online) (a) Detected interference fringe measured using the wavelength scanning method. Fringe pattern from 750 to 770 nm is magnified in the inset. (b) Birefringence obtained using the wavelength scanning method. Experimental results and its linear fit are shown by the black dots and the red solid curve, respectively. For comparison, birefringence obtained from the MZ interferometric method is also shown by the green dashed curve. An 11.9 cm long IMEF was used for the measurement.

interference fringe has a period of about 1 nm, which means a time delay of approximately 1.94 ps between the two fundamental modes at 760 nm after propagating through the IMEF. Figure 8(b) shows the group birefringence B obtained from the relation:

$$B = \frac{\bar{\lambda}^2}{\Delta\lambda L}, \tag{5}$$

where $\Delta\lambda$ is the wavelength difference between the adjacent peaks, and $\bar{\lambda}$ is the corresponding center wavelength. The dots represent the measured values, and the red line is the linear fit. For the sake of contrast, the values of birefringence obtained using the MZ interferometric method are also denoted by the green dashed curve. In the MZ interferometric method, the group birefringence B can be obtained from the time delays between two fundamental modes as the following equation,

$$B = n_s(\lambda) - n_l(\lambda) = \frac{c\{\tau_s(\lambda) - \tau_l(\lambda)\}}{L}, \tag{6}$$

where n_s, n_l, τ_s, and τ_l are the refractive indices and time delays for the short and long axis modes, respectively, and L is the length of the IMEF under test. From the wavelength-dependent values of the time delays, τ_s and τ_l, shown in Fig. 6(b) and the fiber length of 15 cm used in the MZ interferometer shown in Fig. 5, the birefringence of the IMEF can be calculated. The results from these two methods are in good agreement with each other.

As expected, B is very large due to the high ellipticity of the core. The obtained value at 800 nm is $0.0054 \pm 7.5 \times 10^{-4}$ from the wavelength scanning method and $0.0057 \pm 1.7 \times 10^{-4}$ from the MZ interferometric method, and it increases up to 0.0124 at 1500 nm according to the numerical results, which is one order of magnitude larger than the values for usual polarization-maintaining (PM) fibers. The proportionality of the birefringence to the wavelength in the visible and near-infrared region agrees well with the general properties of birefringence of PM-microstructured fibers [19].

As can be seen in Fig. 8(b), the values of the experimental data (black dots) have a step structure, which is due to the discrete data processing of wavelength in the optical spectrum analyzer (OSA), that is, the minimum step in the value of B, $\delta B = (\bar{\lambda}^2)/(\Delta\lambda)^2 L\delta(\Delta\lambda) = B[\delta(\Delta\lambda)/\Delta\lambda]$. For example, at 750 nm, where the fringe pattern is clear, $B = 0.00483$, which is from the linear fit, $\Delta\lambda = 1.08$ nm, and the wavelength resolution of the OSA, $\delta(\Delta\lambda)$, is 0.04 nm; thus δB is 1.79×10^{-4}, which well agrees with the experimental value of 1.855×10^{-4}. In addition, the step gets larger as the wavelength becomes longer, as can be seen in Eq. (5). Therefore, the higher resolution of the wavelength makes the step in the value of B smaller. However, it is observed that the error originating from the experimentally measured interference peak is larger than the error from the wavelength resolution. The group birefringence depicted in Fig. 8(b) has a larger error range in the long wavelength regime than the ZDW regime. It may be due to the nonlinear effect, especially the generation of solitons in the long wavelength regime [4,5]. The MZ interferometric method is better than the wavelength scanning method in getting clear birefringence properties, because only the signal pulse experiences the noise attributable to the nonlinear interaction in the IMEF, whereas both pulses experience it in the case of the wavelength scanning method.

5. Supercontinuum Generation for Application

Finally, we show the SC spectrum applicable to an f–$2f$ interferometric system utilizing the IMEF that we have analyzed. Since the IMEF can also guide the light due to the high index contrast between the core and the cladding regions, and the light is tightly confined in the small core region, the pulse propagating in this IMEF can generate SC spectrum in spite of the irregular structure of the cladding. A 30 fs input pulse with the central wavelength of 830 nm is launched to a 14 cm long IMEF. The output power after passing the IMEF was approximately 30 mW, when the input power is 170 mW. The FI was not employed in this experiment because it brings about temporal broadening of the input pulse. Our Ti:sapphire laser oscillator operated stably even with the backreflected pulses from the IMEF when the temporal width of laser pulses was 30 fs. The spectral components of the output pulses are from 430 to 1300 nm for the long axis mode and from 420 to 1150 nm for the short axis mode, respectively, as can be seen in Fig. 9(a). It is well-known that solitons are generated at the wavelengths longer than the ZDW, that is, 1249 nm for the long axis mode and 1109 nm for the short axis mode. Besides, the resonant waves corresponding to the solitons are generated at the

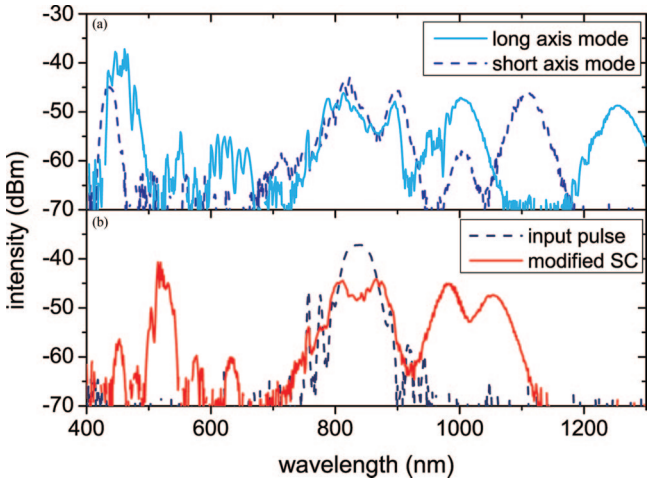

Fig. 9. (Color online) (a) Supercontinuum spectra for the long and short axis modes of the IMEF that we have analyzed are shown in the cyan solid and blue dashed curves, respectively. (b) Spectrum of the input pulse of 30 fs width with 830 nm central wavelength and the modified SC spectrum for an f–$2f$ interferometric system are shown in the blue dashed and red solid curves, respectively.

wavelength shorter than the ZDW, that is, 451 nm for the long axis mode and 436 nm for the short axis mode.

Though these spectra span over one-octave and have f and $2f$ components, that is, approximately 860 nm and approximately 430 nm, we tried to generate spectral components of 1064 and 532 nm because those are the fundamental and the second-harmonic wavelengths of the Nd:YAG laser, which offers convenience for further studies using the f–$2f$ interferometric systems. The SC spectrum depends on many parameters such as the bandwidth, the power and polarization of the input pulse, or the fiber length. In our case, it is enough to rotate the polarization direction of the input pulse using a half-wave plate to generate an applicable one-octave-spanning spectrum. Figure 9(b) shows the spectrum of the 30 fs input pulse and the modified SC spectrum generated by letting the direction of the linearly polarized input pulse oriented at 45° with respect to the principal axes of the IMEF. This shows that the IMEF with an elliptic core offers an easy way of controlling the SC spectrum to generate desirable frequency components.

6. Conclusion

We have investigated the near- and far-field images of the principal modes and dispersion properties of the irregularly microstructured elliptic core fiber. The long and short axes of the elliptic shape of the far-field pattern are rotated by 90° with respect to those of the near-field pattern. The large aspect ratio of the core axes gives rise to the big difference between the two ZDWs and the large value of birefringence. The ZDW is 740 nm for the long axis mode and 683 nm for the short axis mode. The group birefringence is approximately 0.0055 near 800 nm and increases in proportion to the wavelength. In addition, a wide SC spectrum generated with the IMEF with an elliptic core could be applicable for an f–$2f$ interferometric system.

This work was supported by the Ministry of Commerce, Industry, and Energy of Korea through the Industrial Infrastructure Building Program.

References

1. J. C. Knight, "Photonic crystal fibers," Nature (London) **424,** 847–851 (2003).
2. J. K. Ranka, R. S. Windeler, and A. J. Stentz, "Visible continuum generation in air-silica microstructure optical fibers with anomalous dispersion at 800 nm," Opt. Lett. **25,** 25–27 (2000).
3. A. V. Husakou and J. Herrmann, "Supercontinuum generation of higher-order by fission in photonic crystal fibers," Phys. Rev. Lett. **87,** 203901 (2001).
4. S. Coen, A. H. L. Chau, R. Leonhardt, J. D. Harvey, J. C. Knight, W. J. Wadsworth, and P. St. J. Russell, "Supercontinuum generation in air-silica microstructured fibers with nanosecond and femtopulse pumping," J. Opt. Soc. Am. B **19,** 753–764 (2002).
5. D. V. Skryabin, F. Luan, J. C. Knight, and P. St. J. Russell, "Soliton self-frequency shift cancellation in photonic crystal fibers," Science **301,** 1705–1708 (2003).
6. H. Kano and H. Hamaguchi, "Vibrationally resonant imaging of a single living cell by supercontinuum-based multiplex coherent anti-Stokes Raman scattering microspectroscopy," Opt. Express **13,** 1322–1327 (2005).
7. A. D. Aguirre, N. Nishizawa, J. G. Fujimoto, W. Seitz, M. Lederer, and D. Kopf, "Continuum generation in a novel photonic crystal fiber for ultrahigh resolution optical coherence tomography at 800 nm and 1300 nm," Opt. Express **14,** 1145–1160 (2006).
8. Th. Udem, R. Holzwarth, and T. W. Hansch, "Optical frequency metrology," Nature (London) **416,** 233–237 (2002).
9. J. Jasapara, T. H. Her, R. Bise, R. Windeler, and D. J. DiGiovanni, "Group-velocity dispersion measurements in a photonic bandgap fiber," J. Opt. Soc. Am. B **20,** 1611–1615 (2003).
10. A. Gosteva, M. Haiml, R. Paschotta, and U. Keller, "Noise-related resolution limit of dispersion measurements with white-light interferometers," J. Opt. Soc. Am. B **22,** 1868–1873 (2005).
11. J. R. Folkenberg, M. D. Nielsen, N. A. Mortensen, C. Jakobsen, and H. R. Simonsen, "Polarization maintaining large mode area photonic crystal fiber," Opt. Express **12,** 956–960 (2004).
12. X. Chen, M.–J. Li, N. Venkataraman, M. T. Gallanher, W. A. Wood, A. M. Crowley, J. P. Carberry, L. A. Zentano, and K. W. Koch, "Highly birefringent hollow-core photonic bandgap fiber," Opt. Express **12,** 3888–3893 (2004).
13. F. Brechet, J. Marcou, D. Pagnoux, and P. Roy, "Complete analysis of the characteristics of propagation into photonic crystal fibers by the finite element method," Opt. Fiber Technol. **6,** 181–191 (2000).
14. K. Iizuka, *Elements of Photonics* (Wiley-Interscience, 2002).
15. D. Ouzounov, D. Homoelle, W. Zipfel, W. W. Webb, A. L. Gaeta, J. A. West, J. C. Fajardo, and K. W. Goch, "Dispersion measurements of microstructured fibers using femtosecond laser pulses," Opt. Commun. **192,** 219–223 (2001).
16. T. Niemi, M. Uusimaa, and H. Ludvigsen, "Limitations of phase-shift method in measuring dense group delay ripple of fiber Bragg gratings," IEEE Photon. Technol. Lett. **13,** 1334–1336 (2001).
17. G. Genty, M. Lehtonen, H. Ludvigsen, and M. Kaivola, "Enhanced bandwidth of supercontinuum generated in microstructured fibers," Opt. Express **12,** 3471–3480 (2004).
18. M. H. Frosz, P. Falk, and O. Bang, "The role of the second zero-dispersion wavelength in generation of supercontinua and bright-bright soliton-pairs across the zero-dispersion wavelength," Opt. Express **16,** 6181–6192 (2005).
19. T. P. Hansen, J. Broeng, S. E. B. Libori, E. Knudsen, A. Bjarklev, J. R. Jensen, and H. Simonsen, "Highly birefringent index-guiding photonic crystal fibers," IEEE Photon. Technol. Lett. **13,** 588–590 (2001).